NANO LETTERS

pubs.acs.org/NanoLett

Surface Energies Control the Self-Organization of Oriented In_2O_3 Nanostructures on Cubic Zirconia

Kelvin H. L. Zhang,[†] Aron Walsh,[‡] C. Richard A. Catlow,[‡] Vlado K. Lazarov,[§] and Russell G. Egdell*[,†]

[†]Department of Chemistry, Chemistry Research Laboratory, University of Oxford, 12 Mansfield Road, Oxford, OX1 3TA, United Kingdom, [‡]Materials Chemistry, Department of Chemistry, University College London, Third Floor, Kathleen Lonsdale Building, Gower Street, London, WC1E 6BT, United Kingdom, and [§]Department of Physics, University of York, Heslington, York, YO10 5DD, United Kingdom

ABSTRACT Highly aligned one-dimensional (1D) nanorods of the transparent conducting oxide In_2O_3 have been grown on (110)-oriented Y-stabilized ZrO_2 substrates, whereas growth on (100) and (111) substrates leads respectively to blocklike 3D islands and continuous films. It is shown that the striking influence of substrate orientation on the growth morphology is controlled by differences in energies between the low index surfaces of In_2O_3 and that spontaneous self-organization is driven by minimization of surface energies.

KEYWORDS Transparent conducting oxides, In_2O_3, self-organization, nanostructures

Transparent conducting oxides (TCOs) are key materials when it is necessary to combine optical transparency in the visible region with a high electrical conductivity.[1] In_2O_3 doped with Sn (widely, but somewhat misleadingly, known as indium tin oxide or ITO) is one of the most important TCOs due to its intrinsically facile dopability, high conductivity, excellent transparency, and easy processability.[2,3] Despite the fact that ITO finds widespread application in liquid crystal displays, solar cells and other optoelectronic devices, the basic physical properties of the material have been the subject of ongoing controversy. For example, it was only in 2008 that it was established that In_2O_3 has a direct, but dipole forbidden, bandgap of around 2.8 eV, almost 1 eV lower than the widely quoted value of 3.75 eV which marks the onset of fully allowed optical transitions.[4] Revision of the value for the bandgap led in turn to the realization that electron accumulation may be observed on In_2O_3 surfaces with low bulk doping levels.[5] The renewed interest in the bulk and surface physics of In_2O_3 has encouraged attempts to grow high quality single crystal thin films of In_2O_3 both for detailed fundamental investigations and for electronic device applications.[6−13] There has also been an interest ongoing over many years in preparation of nanostructured In_2O_3 using solution techniques based on sol−gel or solvothermal processing,[14−16] chemical vapor deposition,[17,18] and electron beam evaporation.[19] Nanostructured In_2O_3 has potential applications in gas sensing, field emission devices, and transparent electronics. A general limitation of the earlier approaches, however, is that they provide no control over the orientation of the structures formed. In the current work, we demonstrate that growth of In_2O_3 by high-temperature oxygen plasma-assisted molecular beam epitaxy (MBE) opens the possibility of rational design of highly oriented nanostructured films. Self-organization arising from lattice mismatch during heteroepitaxial growth provides a well-established approach to the preparation of "quantum dots" in conventional semiconductor systems such as Ge on Si and InAs on GaAs; the morphology of the dots is determined by an interplay between elastic strain and surface energies.[20,21] Much less effort has been devoted to the controlled self-assembly of oxide nanostructures during epitaxial growth.[22] Oxides and other polar materials are however of particular interest because in general there are very large differences between the energies of different low-index surfaces. This provides a means to control the aspect ratio and orientation of nanostructured material. Specifically, we explore the influence of substrate orientation in the epitaxial growth of In_2O_3 on Y-stabilized cubic ZrO_2 (YSZ).

In_2O_3 adopts a body-centered cubic bixbyite structure with space group $Ia\bar{3}$ and lattice parameter $a = 1.01170$ nm. The structure may be regarded as a $2 \times 2 \times 2$ superstructure of fluorite, with ordered removal of O from one-fourth of the anion sites. YSZ adopts a fluorite structure belonging to the space group $Fm\bar{3}m$ with lattice parameter $a = 0.51423$ nm at the 17% Y doping level of the substrates used in the current work. Thus, there is a mismatch of only 1.6% between $2a$ for Y-doped ZrO_2 (1.02846 nm) and a for In_2O_3. Moreover, the

*To whom correspondence should be addressed. E-mail: russell.egdell@chem.ox.ac.uk.

Received for review: 07/9/2010
Published on Web: 08/18/2010

DOI: 10.1021/nl102403t | *Nano Lett.* **2010,** *10,* 3740–3746

cation arrays within the two materials are very similar, minimizing the chemical mismatch at the interface. We demonstrate the spontaneous formation of highly directional one-dimensional (1D) nanorods during high-temperature epitaxial growth of In_2O_3 on (110)-oriented Y-stabilized cubic ZrO_2 (YSZ). By contrast, growth on (100) surfaces leads to truncated square pyramidal islands.[9,12] There is a growing consensus that (111)-oriented substrates are optimal for growth of high quality continuous thin films at relatively low temperature ($T \leq 700$ °C);[10,12,13] we confirm here that atomically flat mesa or continuous thin films develop on (111)-oriented substrates even under high-temperature conditions. On the basis of ab initio quantum chemical simulations, it is shown that the different growth modes and the striking azimuthal orientation of the rods and pyramids on (110) and (100) surfaces are determined by large differences in the energies of the three low index surfaces.

Experimental Section. The In_2O_3 thin films were grown on (100)-, (110)-, and (111)-oriented 1 cm × 1 cm Y-stabilized ZrO_2 substrates in an ultrahigh vacuum oxide MBE system (SVT, U.S.A.) with a base pressure of 5×10^{-10} mbar. This incorporated a hot lip indium Knudsen cell and a radio frequency (RF) plasma oxygen atom source operated at 200 mW RF power with an oxygen background pressure of 3×10^{-5} mB. Substrates were heated radiatively using a graphite filament The nominal growth rate was 0.035 nm s^{-1}, calibrated using the thickness from HRTEM measurements and AFM images. The Y-ZrO_2 substrates were cleaned by exposure to the oxygen atom beam at a nominal substrate temperature of 900 °C. We explored a wide range of growth conditions in terms of film thickness and growth temperature, which ranged between 550 and 1000 °C. Most of the data reported here relate to a deposition time of 3000 s that corresponds to a film thickness of 100 nm assuming a layer growth mode. In situ LEED was carried out in an analysis chamber connected to the growth chamber. AFM images were recorded ex situ with a Digital Instruments Multimode SPM instrument. This was operated in contact mode with a "J" scanner having a lateral range of approximately 100 μm and a vertical range of 6 μm. Silicon nitride probes (Nascatec GmbH model NST NCHFR) with a thin coating of gold to act as a mirror for the laser beam were used. Calibration of the AFM was accomplished by scanning a 10 mm pitch 200 nm 3D reference from Digital instruments. Digital Nanoscope software (version 5.12) was used to analyze and process the AFM topographic images. All the images were treated with the "flatten" command and are presented using one of the standard color palettes of the Nanoscope software. Specimens for cross-sectional TEM were prepared by cutting and mechanical grinding down to 5−10 μm, followed by thinning to electron transparency by Ar ion beam milling using a Gatan 691 Precision Ion Polishing System (PIPS). It proved very difficult to obtain sections with a uniform thickness across the ZrO_2/In_2O_3 interfaces because the epilayer etched at a much higher rate than the substrate. Cross-sectional

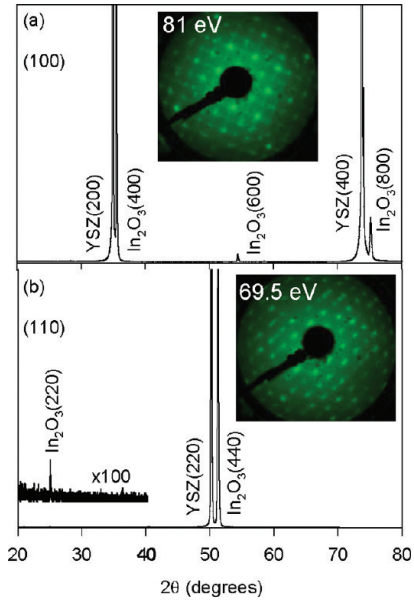

FIGURE 1. $\theta-2\theta$ X-ray diffraction profiles of In_2O_3 films with a nominal thickness of 100 nm grown on (a) (100)- and (b) (110)-oriented Y-stabilized cubic zirconia wafers. The insets show corresponding LEED patterns measured in situ in the MBE growth system.

TEM images were collected using a JEOL3000F microscope operating at 300 keV. Digital Micrograph image software was used to process the TEM images. Bragg filtering was applied to the TEM images to remove some of the background noise and contrast adjustment was applied uniformly across the images where necessary to enhance the display quality.

The bulk and surface electronic structure and total energies were calculated using density functional theory within the generalized gradient approximation (PBE)[23] as implemented in the VASP package.[24,25] The plane-wave kinetic energy threshold (500 eV) and k-point density (4 × 4 × 4) were both well-converged for the bulk system. Starting from the relaxed bulk bixbyite lattice ($a = 1.030$ nm), 2D surface models were constructed using a periodic arrangement of slabs, separated with a 2 nm vacuum region. Convergence of γ with respect to slab thickness resulted in models containing 32, 32, and 48 formula units for the (100), (110), and (111) surfaces, respectively. In all cases, the top two ionic layers were allowed to relax, while all other layers were held at their bulk lattice positions. Simulated annealing was performed to assess the stability of the resulting structures at 750 K and no further relaxations or reconstructions were found to occur.

Figure 1 shows $\theta-2\theta$ X-ray diffraction (XRD) profiles of In_2O_3 films with a nominal thickness of 100 nm grown with a substrate temperature of 750 °C on (100) and (110)-oriented wafers; samples grown at higher temperatures gave similar XRD profiles. In each case, there is near perfect texture in the films and the atomic planes in the epilayer faithfully follow those of the substrate. As reported elsewhere, perfect texture is also observed for growth on (111)-oriented substrates.[13] Epilayer peaks with doubled Miller

DOI: 10.1021/nl102403t | Nano Lett. 2010, 10, 3740–3746

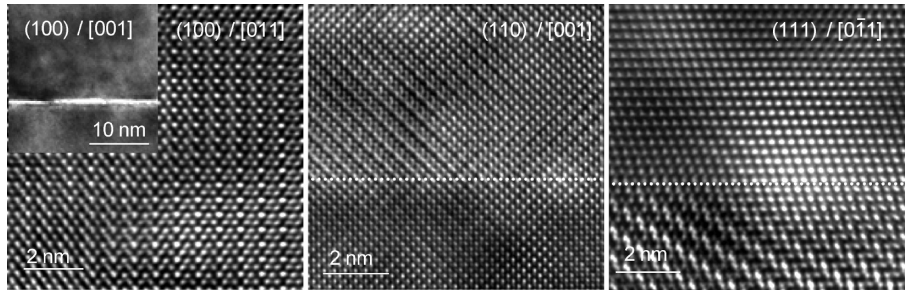

FIGURE 2. High-resolution cross-sectional transmission electron microscopy images of In_2O_3 grown on (100), (110), and (111)-oriented Y-stabilized zirconia substrates, viewed down [011], [001], and [1$\bar{1}$0] directions, respectively. The interface is included in images of the (110) and (111) samples (but not the (100) sample) and is indicated by a dotted line. The inset to the image for the (100) epilayer shows an image of the epilayer/substrate interface viewed down the alternative high symmetry [001] direction.

indices appear close to the substrate (200) and (400) peaks for samples grown on (100)-oriented wafers, but in addition the body-centered cubic structure of In_2O_3 allows for the appearance of a very weak (600) epilayer peak with no nearby (300) substrate peak owing to the face centered cubic structure of stabilized zirconia. For (110) substrate orientation, a single (440) epilayer peak is observed close to the substrate (220) reflection. Within the space group $Ia\bar{3}$ ($hk0$) reflections with $h = k$ are systematically absent unless $h = 2n$, so that the (110) and (330) epilayer peaks are not observed but the (220) peak is observable just above the baseline noise. The insets in Figure 1 show low-energy electron diffraction (LEED) patterns from the differently oriented films measured in situ in the MBE system. As expected the patterns from (100) and (110) surfaces show 4-fold and 2-fold rotational symmetries, respectively. However, the patterns show evidence of streaking and spot splitting that varies strongly with beam energy. This is indicative of extensive faceting at the surface. By contrast the 3-fold symmetric LEED patterns from (111)-oriented films show no evidence of spot splitting.[13]

High-resolution transmission electron microscopy (HR-TEM) images such as those as shown in Figure 2 confirm the excellent crystalline order in the films grown on the three differently oriented substrates and also demonstrate the formation in each case of sharp interfaces between the substrate and the epilayer. However, very pronounced morphological differences between films grown on the different low index substrates are apparent on a longer length scale. The differences are most obvious in large area atomic force microscopy (AFM) images, such as those shown in Figure 3. The (100)-oriented epilayer grown at 750 °C (Figure 3a) is seen to consist of an array of square or rectangular islands with lateral dimensions typically of the order of 100 nm and with edges all aligned parallel to the [011] directions of the substrate. Elongation of the islands takes place along both [011] and [0$\bar{1}$1] directions. The (110) epilayer (Figure 3b) shows a similar island structure but in this case the islands are all rectangular and oriented with edges along [1$\bar{1}$0] and [001] directions. The elongation is exclusively along the [1$\bar{1}$0] direction. By contrast the (111) epilayer consists of larger loosely connected mesa (shown in Figure 3c) with dimensions up to about 5 μm, dissected occasionally by deep troughs which extend down to the substrate. These mesa have a distinctive serrated "autumn leaf" morphology and flat surfaces on which it is possible to resolve atomic scale steps with a height of 0.29 nm. This distance is equal to $a/2\sqrt{3}$ where a is the cubic lattice parameter of In_2O_3 and corresponds to the separation between successive cation containing planes within the bixbyite structure. The morphological differences between (100) and (110) surfaces become even more pronounced for samples grown at 900 °C, as shown in Figure 3d,e. Here the islands on the (100) surface have developed a more uniform square shape. The typical edge size of the islands is now about 1 μm, which is around a factor of 10 bigger than for films grown at 750 °C. The island size is dependent on the surface coverage (Supporting Information). However, the islands always remain aligned with edges parallel to ⟨110⟩ directions and have sloping side facets inclined at 54.7° to the surface plane, evident in both AFM images and cross sectional TEM. The characteristic angle and the azimuthal orientation allow us to identify the side facets as being of {111} origin. As shown in Figure 3e, on the (110) surface the anisotropy between [1$\bar{1}$0] and [001] directions becomes much more apparent and the islands have assumed a "rodlike" appearance with typical lengths between 2 and 5 μm along the [1$\bar{1}$0] direction but with widths of around only 100 nm along the [001] direction. In contrast to films grown on (100) and (110) substrates, those grown on (111) substrates showed very little change on increasing the growth temperature from 750 to 900 °C (Figure 3f). The spontaneous development of highly oriented nanorods on (110) surfaces prompted us to explore growth at yet higher temperatures. Panels g–i in Figure 3 show AFM images of a layer grown with a lower nominal coverage (50 nm) than in Figure 3e at 1000 °C. The rods are now further elongated with lengths in excess of 20 μm and a width restricted to about 100 nm, to give an aspect ratio of over 200. As with the square islands on (100) surfaces, the rods have sloping side facets and the predominant facets parallel to the [1$\bar{1}$0] direction are of {111} nature.

The morphology of growth in mismatched epitaxial systems depends on a complex interplay between the kinetics of

DOI: 10.1021/nl102403t | *Nano Lett.* **2010,** *10,* 3740–3746

FIGURE 3. Atomic force microscopy (AFM) images of In_2O_3 grown on oriented Y-stabilized zirconia substrates. The images in (a−c) are for samples grown at 750 °C substrate temperature on (100), (110), and (111)-oriented substrates, respectively, while the images in (d−f) are for samples grown at 900 °C substrate temperature. The main images are scanned over an area of 20 μm × 20 μm and give an indication of the overall topology. The insets show scans over a smaller area of 1 μm × 1 μm, except for the inset to (c), which shows a scan over a smaller area of 0.5 μm × 0.5 μm to highlight atomic scale steps. Panels (g−i) show images of nanorods grown on (110)-oriented substrates at 1000 °C with a nominal coverage (50 nm) that is half that in (e). The inset to (i) shows a false 3D view of the AFM image.

nucleation and surface diffusion and the minimization of surface and interface energies and elastic strain. The very pronounced changes with substrate temperature indicate that at low temperatures kinetic factors must be important and it is not clear that even at the highest temperatures that growth morphology is determined by purely thermodynamic factors. Nonetheless, many aspects of the experimental observations can be rationalized by considering the energies of the low-index surfaces of In_2O_3 computed using ab initio total energy calculations. The surface energy (γ) is defined as the energy per unit area required for forming the surface relative to the bulk and is calculated according to:

$$\gamma = (U_{slab} - U_{bulk})/2A$$

where U_{slab} is the total energy of the 2D surface slab with a 2 nm vacuum region and U_{bulk} is the energy of the corresponding number of bulk In_2O_3 formula units; A represents the surface area which is created on each side of the slab and is repeated periodically. The (100), (110), and (111) surfaces were modeled using $a \times a$, $a \times a\sqrt{2}$, and $a\sqrt{2} \times a\sqrt{2}$ expansions, respectively.

Side view ball and stick models of the three bixbyite surfaces are shown in Figure 4 along with corresponding views of the low-index fluorite surfaces. The computed relaxed surface energies and associated relaxation energies are given at the bottom of the figure. The (100) surface of fluorite is a classic example of a "Type III" ionic surface within the Tasker classification[26] and contains alternating cation and anion planes. These give rise to a surface dipole and cause the surface energy to diverge to infinity for sufficiently thick slabs. The polar surface may be stabilized in a simple manner through microfaceting,;[27,28] that is, by transferring half the ions in the outermost ionic layer to the other side of the slab, which allows for distinct cation- or anion-terminated surfaces. By contrast, the (110) surface of

DOI: 10.1021/nl102403t | *Nano Lett.* **2010,** *10,* 3740–3746

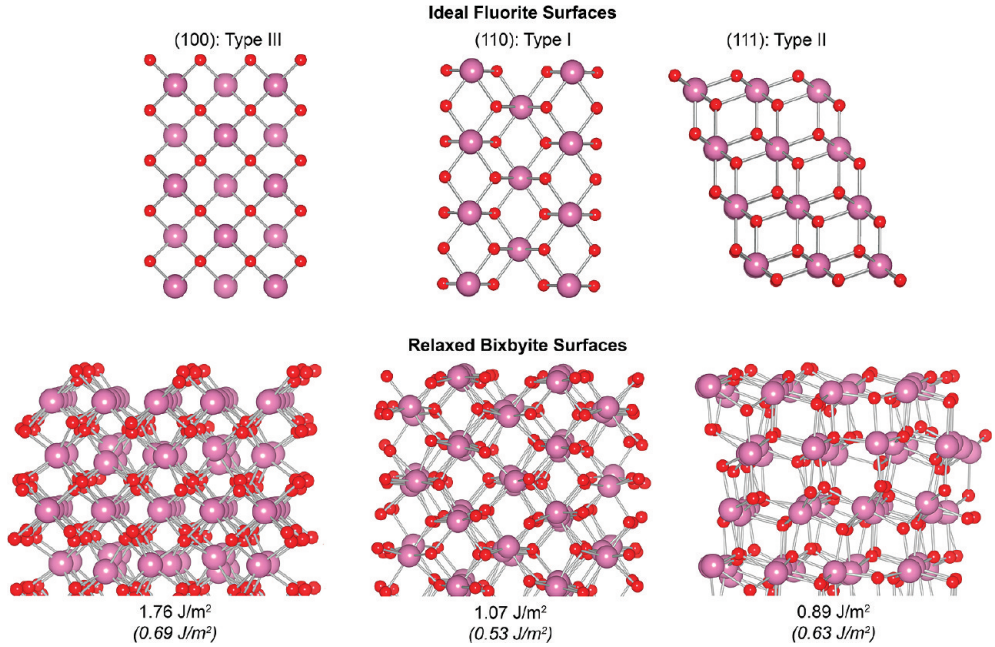

FIGURE 4. Ball and stick representations of the pristine low-index terminations of the fluorite (AB_2) and the relaxed In_2O_3 bixbyite (A_2B_3) surface structures, which are labeled according to the Tasker surface notation for polar compounds. The anions and cations are represented by large and small spheres, respectively. The relaxed surface energies are given for each termination along with the relaxation energy in parentheses.

fluorite is a stable "Type I" surface containing charge neutral ionic layers. Finally the (111) surface is "Type II" and contains repeating quadrupolar grouping of anionic and cationic layers. The bixbyite surfaces of In_2O_3 are very similar in appearance to those of the parent fluorite structure, although there is minor rumpling within the cation layers due to the relaxations in atomic positions associated with the intrinsic vacant oxygen sites within the structure and the (110) surface is no longer rigorously "Type II". The bulk-terminated surface energies follow a sequence $\gamma(100)_{In} > \gamma(100)_O > \gamma(110) > \gamma(111)$, although the difference between (111) and (110) surfaces is rather small. However, the relaxation energy for the (111) surface is significantly bigger than for the (110) surface so that the relaxed surface energy for the (111) surface is about 0.18 J/m^2 lower than the (110) surface energy. Cleavage of the (111) surface breaks a single long In−O bond (0.24 nm) separating the charge neutral In_2O_3 units; efficient relaxation is then achieved primarily through a concerted contraction of the ⟨111⟩ In−O bond in the subsurface layers by ca. 9%. The order of surface energies is the same as found for oxides with the fluorite structure such as UO_2[28] and our substrate material cubic Y-stabilized ZrO_2.[29,30] Thus for 24% Y-doped ZrO_2, Ballabio et al.[29] found relaxed surface energies $\gamma(100) = 1.75$ J/m^2, $\gamma(110) = 1.44$ J/m^2, and $\gamma(111) = 1.04$ J/m^2. Note however that the order of surface energies for In_2O_3 is different from that proposed by Hao et al. who suggested a sequence $\gamma(110) > \gamma(100) > \gamma(111)$ on the basis of the morphologies In_2O_3 nanocrystals prepared by vapor transport.[31]

The present results establish unambiguously that the surface energies of In_2O_3 have a direct influence on the morphology of single crystal thin films. Continuous or near continuous epilayers that are atomically flat on the micrometer length range can be grown under a wide range of conditions on (111)-oriented substrates because the (111) surface energy for In_2O_3 is the lowest among the three low index surfaces and $\gamma_{In2O3}(111) < \gamma_{Y\text{-}ZrO2}(111)$. By contrast on (100) and (110) surfaces an island growth mode is preferred. The thermodynamically favored (111) termination is found to occur through spontaneous development of sloping side facets on the islands. Although this increases the surface area of side facets by a factor of cosec θ (where θ is the contact angle with the surface), this is energetically favorable because higher energy {110} or {100} edge walls are replaced by lower energy {111} facets. In addition there is a reduction in the surface energy associated with the island top and with the bare substrate at the minimal expense of increasing the overall contribution of the interface energy.

The propensity for the sloping side facets of the islands to have {111} orientation in turn determines the azimuthal orientation of the square islands found on (100) substrates and the elongation of islands along the $[1\bar{1}0]$ direction to give rodlike structures on (110)-oriented substrates. This is illustrated in Figure 5 that shows that {111} side facets can form on (100) islands provided the island edges align along ⟨110⟩ directions; alignment with edges parallel to ⟨100⟩ directions would be associated with higher energy {110} side facets. Similarly on (110) surfaces, elongation of islands to give rodlike structures with the long axis along the $[1\bar{1}0]$ direction allows for the development of extended {111} side facets whereas elongation along the [001] direction would demand formation of extended sloping {100} facets. A

DOI: 10.1021/nl102403t | *Nano Lett.* **2010,** *10,* 3740–3746

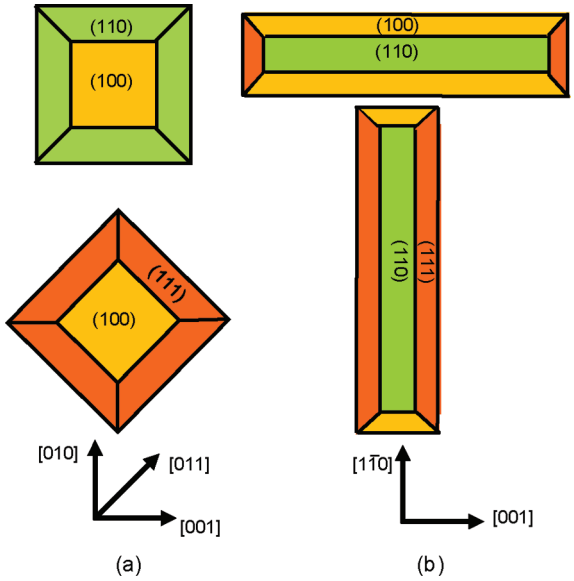

FIGURE 5. Schematic plan view illustrating the influence of azimuthal orientation on the facets that can develop on In_2O_3 islands grown on (a) (100)- and (b) (110)-oriented Y-ZrO_2 substrates. The preferred orientations shown in the two lower schematics allow development of thermodynamically favored {111} side facets.

detailed treatment of the orientation dependence of the surface energy of the square islands found on (100) surfaces is given as Supporting Information; it is found that an energy of order 3.8×10^{-13} J is required to rotate an island of the sort shown in Figure 3d through 45°. Furthermore, it is shown that the formation of nanorod islands with a very high aspect ratio between length l and width w is driven by minimization of the surface energy, provided that the interface energy $\gamma_i(110)$ is small.

In summary, we have been able to rationalize both the distinct growth modes found for In_2O_3 on differently oriented Y-stabilized zirconia surfaces and the propensity for development of islands with {111} facets on (100) and (110) surfaces in terms of relaxed surface energies. The growth of highly oriented nanorods on (110) substrates is of particular note given the growing recent interest in field effect transistors based on nanowires.[32−34] However, most established techniques for preparation of oxide nanowires[35−37] or nanobelts[35] lead to a tangled mass of interpenetrating structures, which is in contrast to the perfectly aligned rods prepared in the present work. The use of an anisotropic (110) substrate as in the present work ensures that the rods align spontaneously in one direction. This is in contrast to very recent work[38] where Gd-doped CeO_2 nanorods were grown on the (100) surface of cubic $LaAlO_3$. Here the formation of (110)-oriented rodlike structures is driven by anisotropy in the mismatch between the square surface cell of the substrate and the rectangular surface cell of the epilayer. However, rods grow in two orthogonal directions unless the substrate is deliberately scratched to promote uniaxial growth. We can conclude that the use of slightly mismatched (110)-oriented substrates of cubic or tetragonal materials will provide a general approach to the epitaxial growth of oxide nanostructures with uniaxial orientation.

Acknowledgment. The Oxford MBE programme was funded by EPSRC Grant ES/94148. K.H.L.Z. is grateful to Oxford University for the award of a Clarendon Scholarship. A.W. would like to acknowledge funding from a Marie-Curie Intra-European Fellowship from the European Union. Via membership of the UK's HPC Materials Chemistry Consortium funded by EPSRC grant EP/F067496, this grant made use of the facilities of HECToR, the UK's high-performance computing service.

Supporting Information Available. (S1) Control of the In_2O_3 island size on (100) surfaces; (S2) analysis of island orientation on (100) surfaces; (S3) aspect ratio of nanorods on (110)-oriented substrates. This material is available free of charge via the Internet at http://pubs.acs.org.

REFERENCES AND NOTES

(1) Thomas, G. *Nature* **1997**, *389*, 907–908.
(2) Edwards, P. P.; Porch, A.; Jones, M. O.; Morgan, D. V.; Perks, R. M. *Dalton Transactions* **2004**, 2995–3002.
(3) Granqvist, C. G.; Hultaker, A. *Thin Solid Films* **2002**, *411*, 1–5.
(4) Walsh, A.; Da Silva, J. L. F.; Wei, S. H.; Korber, C.; Klein, A.; Piper, L. F. J.; DeMasi, A.; Smith, K. E.; Panaccione, G.; Torelli, P.; Payne, D. J.; Bourlange, A.; Egdell, R. G. *Phys. Rev. Lett.* **2008**, *100*, No. 167402-1−4.
(5) King, P. D. C.; Veal, T. D.; Payne, D. J.; Bourlange, A.; Egdell, R. G.; McConville, C. F. *Phys. Rev. Lett.* **2008**, *101*, No. 116808-1−4.
(6) Ohta, H.; Orita, M.; Hirano, M.; Hosono, H. *J. Appl. Phys.* **2002**, *91*, 3547–3550.
(7) Koida, T.; Kondo, M. *J. Appl. Phys.* **2006**, *99*, No. 123703-1−9.
(8) Bourlange, A.; Payne, D. J.; Egdell, R. G.; Foord, J. S.; Edwards, P. P.; Jones, M. O.; Schertel, A.; Dobson, P. J.; Hutchison, J. L. *Appl. Phys. Lett.* **2008**, *92*, No. 092117-1−3.
(9) Bourlange, A.; Payne, D. J.; Jacobs, R. M. J.; Egdell, R. G.; Foord, J. S.; Schertel, A.; Dobson, P. J.; Hutchison, J. L. *Chem. Mater.* **2008**, *20*, 4551–4553.
(10) Morales, E. H.; He, Y. B.; Vinnichenko, M.; Delley, B.; Diebold, U. *New J. Phys.* **2008**, *10*, No. 125030-1−10.
(11) Morales, E. H.; Diebold, U. *Appl. Phys. Lett.* **2009**, *95*, 253105.
(12) Bierwagen, O.; White, M. E.; Tsai, M. Y.; Speck, J. S. *Appl. Phys. Lett.* **2009**, *95*, 262105-1−3.
(13) Zhang, K. H. L.; Payne, D. J.; Palgrave, R. G.; Lazarov, V. K.; Chen, W.; Wee, A. T. S.; McConville, C. F.; King, P. D. C.; Veal, T. D.; Panaccione, G.; Lacovig, P.; Egdell, R. G. *Chem. Mater.* **2009**, *21*, 4353–4355.
(14) Kim, K. Y.; Park, S. B. *Mater. Chem. Phys.* **2004**, *86*, 210–221.
(15) Wang, C. Q.; Chen, D. R.; Jiao, X. L.; Chen, C. L. *J. Phys. Chem. C* **2007**, *111*, 13398–13403.
(16) Wang, C. Q.; Chen, D. R.; Jiao, X. L. *J. Phys. Chem. C* **2009**, *113*, 7714–7718.
(17) Singh, N.; Zhang, T.; Lee, P. S. *Nanotechnology* **2009**, *20*, No. 195605-1−7.
(18) Yan, Y. G.; Zhang, Y.; Zeng, H. B.; Zhang, L. D. *Cryst. Growth Des.* **2007**, *7*, 940–943.
(19) Wan, N.; Xu, J.; Chen, G. R.; Gan, X. H.; Guo, S. H.; Xu, L.; Chen, K. J. *Acta Mater.* **2010**, *58*, 3068–3072.
(20) Stangl, J.; Holy, V.; Bauer, G. *Rev. Mod. Phys.* **2004**, *76*, 725–783.
(21) Barth, J. V.; Costantini, G.; Kern, K. *Nature* **2005**, *437*, 671–679.
(22) Zheng, H.; Wang, J.; Lofland, S. E.; Ma, Z.; Mohaddes-Ardabili, L.; Zhao, T.; Salamanca-Riba, L.; Shinde, S. R.; Ogale, S. B.; Bai, F.; Viehland, D.; Jia, Y.; Schlom, D. G.; Wuttig, M.; Roytburd, A.; Ramesh, R. *Science* **2004**, *303*, 661–663.
(23) Perdew, J. P.; Burke, K.; Ernzerhof, M. *Phys. Rev. Lett.* **1996**, *77*, No. 3865-1−4.

DOI: 10.1021/nl102403t | *Nano Lett.* **2010,** *10,* 3740–3746

(24) Kresse, G.; Furthmuller, J. *Phys. Rev. B* **1996**, *54*, 11169–11186.
(25) Kresse, G.; Joubert, D. *Phys. Rev. B* **1999**, *59*, 1758–1775.
(26) Tasker, P. W. *J. Phys. C: Solid State Phys.* **1979**, *12*, 4977–4984.
(27) Watson, G. W.; Kelsey, E. T.; deLeeuw, N. H.; Harris, D. J.; Parker, S. C. *J. Chem. Soc., Faraday Trans.* **1996**, *92*, 433–438.
(28) Skomurski, F. N.; Ewing, R. C.; Rohl, A. L.; Gale, J. D.; Becker, U. *Am. Mineral.* **2006**, *91*, 1761–1772.
(29) Ballabio, G.; Bernasconi, M.; Pietrucci, F.; Serra, S. *Phys. Rev. B* **2004**, *70*, No. 075417-1−6.
(30) Lallet, F.; Olivi-Tran, N.; Lewis, L. J. *Phys. Rev. B* **2009**, *79*, No. 035413-1−12.
(31) Hao, Y. F.; Meng, G. W.; Ye, C. H.; Zhang, L. D. *Cryst. Growth Des.* **2005**, *5*, 1617–1621.
(32) Lauhon, L. J.; Gudiksen, M. S.; Wang, C. L.; Lieber, C. M. *Nature* **2002**, *420*, 57–61.
(33) Ju, S. Y.; Facchetti, A.; Xuan, Y.; Liu, J.; Ishikawa, F.; Ye, P. D.; Zhou, C. W.; Marks, T. J.; Janes, D. B. *Nat. Nanotechnol.* **2007**, *2*, 378–384.
(34) Nilsson, H. A.; Caroff, P.; Thelander, C.; Lind, E.; Karlstrom, O.; Wernersson, L. E. *Appl. Phys. Lett.* **2010**, *96*, 153505-1−3.
(35) Pan, Z. W.; Dai, Z. R.; Wang, Z. L. *Science* **2001**, *291*, 1947–1949.
(36) O'Dwyer, C.; Szachowicz, M.; Visimberga, G.; Lavayen, V.; Newcomb, S. B.; Torres, C. M. S. *Nat. Nanotechnol.* **2009**, *4*, 239–244.
(37) Noriega, R.; Rivnay, J.; Goris, L.; Kalblein, D.; Klauk, H.; Kern, K.; Thompson, L. M.; Palke, A. C.; Stebbins, J. F.; Jokisaari, J. R.; Kusinski, G.; Salleo, A. *J. Appl. Phys.* **2010**, *107*, No. 074312-1−7.
(38) Zabaleta, J.; Mestres, N.; Abellan, P.; Gibert, M.; Sandiumenge, F.; Puig, T.; Obradors, X. *Nanotechnology* **2010**, *21*, No. 025302-1−8.

DOI: 10.1021/nl102403t | *Nano Lett.* **2010,** *10,* 3740--3746